JOURNAL OF GEOPHYSICAL RESEARCH, VOL. 114, B03308, doi:10.1029/2007JB005568, 2009

Physical properties of subducted slab and surrounding mantle in the Izu-Bonin subduction zone based on Broadband Ocean Bottom Seismometer data

Azusa Shito,[1] Hajime Shiobara,[1] Hiroko Sugioka,[2] Aki Ito,[2] Yasuko Takei,[1] Hitoshi Kawakatsu,[1] and Toshihiko Kanazawa[1]

Received 25 December 2007; revised 22 October 2008; accepted 1 December 2008; published 24 March 2009.

[1] Seismic attenuation and traveltime anomalies in the vicinity of the Izu-Bonin subduction zone are inferred from waveform data recorded by Broadband Ocean Bottom Seismometers (BBOBSs) deployed as part of the Stagnant Slab Project. We measure the path-averaged attenuation of P waves and traveltime anomalies of both P and S waves using waveform data from 10 regional earthquakes within the Izu-Bonin slab. The observed relation between the attenuation and traveltime anomalies is quantitatively evaluated on the basis of mineral physics. For the data that sample the slab and the Pacific mantle beneath the slab, the relation between the attenuation and traveltime anomalies is consistent with predictions based on the thermal effect. The data that sample the mantle wedge show pronounced positive traveltime anomalies unaccompanied by comparable high attenuation. The traveltime anomalies are too intense to be explained solely in terms of the temperature effect. The temperature anomalies estimated from attenuation suggest that the temperature in the mantle wedge reaches the dry solidus of peridotite. The relative intensity of S to P wave traveltime anomalies of mantle wedge data, after correction for the thermal effect, is relatively small ($R_{S/P}$ = 0.5–1.2). Similarly low-velocity anomalies without comparable high attenuation and with relatively small $R_{S/P}$ (<1.5) have been reported in previous studies of subduction zones at Tonga, in the southwest Pacific, and Tohoku, Japan. We discuss to what extent the present seismological observations can be explained by partial melt on the basis of recent theoretical and experimental studies on partially molten rocks.

Citation: Shito, A., H. Shiobara, H. Sugioka, A. Ito, Y. Takei, H. Kawakatsu, and T. Kanazawa (2009), Physical properties of subducted slab and surrounding mantle in the Izu-Bonin subduction zone based on Broadband Ocean Bottom Seismometer data, *J. Geophys. Res.*, *114*, B03308, doi:10.1029/2007JB005568.

1. Introduction

[2] Subduction zones represent one of the most active sites of volcanism on Earth, where primary processes of physical and chemical evolution occur. To understand the dynamics of subduction zones, it is important to estimate the various parameters (e.g., temperature, chemical composition, and melt fraction) that control magmatism. In this regard, a key approach is quantitative interpretations of seismological observations based on knowledge of mineral physics [*Shito et al.*, 2006].

[3] Although both seismic attenuation and velocity are affected by temperature and partial melt, the relative magnitudes of these effects may vary [*Faul et al.*, 2004; *Hammond and Humphreys*, 2000a, 2000b]. Consequently, a comparison of attenuation and velocity would help to constrain the existence of partial melt, distinct from a temperature anomaly. In addition, the relative magnitudes of S and P wave velocity anomalies can be used to constrain the origin of a particular velocity anomaly [*Karato and Karki*, 2001; *Takei*, 2002].

[4] Along the Izu-Bonin subduction zone, the Pacific plate is subducting beneath the Philippine Sea plate, with active volcanism within the trench (Figure 1). *Shito et al.* [2006] reported the three-dimensional distribution of temperature, water content, and Mg/(Mg + Fe) content in the upper mantle beneath the Philippine Sea based on tomography employing P and S wave velocities [*Gorbatov and Kennett*, 2003] and P wave attenuation [*Shito and Shibutani*, 2003]; however, a lack of seismic stations meant that the spatial resolution and coverage of the tomography (especially for the attenuation tomography) were insufficient for detailed analysis in the vicinity of the Izu-Bonin subduction zone.

[5] Broadband Ocean Bottom Seismometers (BBOBSs) were temporarily deployed in the Philippine Sea and western Pacific Ocean from October 2005 to November 2006, providing the first opportunity to simultaneously study

[1] Earthquake Research Institute, University of Tokyo, Tokyo, Japan.
[2] Institute for Research on Earth Evolution, JAMSTEC, Kanagawa, Japan.

0148-0227/09/2007JB005568$09.00

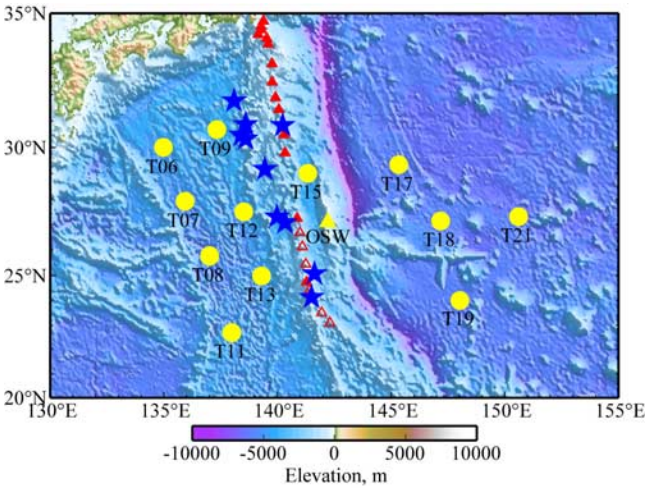

Figure 1. Topographic map of the Izu-Bonin subduction zone. Circles represent BBOBS stations, and the large triangle represents the OSW F-net station. Stars represent seismic events. Solid and open small triangles represent volcanic islands and submarine volcanoes, respectively. Bathymetry data are from ETOPO5 (NOAA National Geophysical Data Center).

seismic attenuation and velocity in the vicinity of the Izu-Bonin subduction zone. The present analysis of BBOBS data provides new understanding of the seismic properties of the region, which cannot be obtained from data collected at land stations.

[6] In this paper, we use BBOBS experimental data, in combination with the results of recent theoretical and experimental studies in mineral physics, to quantitatively investigate the relations between (1) P wave attenuation and P wave traveltime anomaly and (2) P wave and S wave traveltime anomalies, with the overall aim of exploring the spatial distributions of temperature and partial melt, which control subduction zone magmatism.

2. Data

[7] The data analyzed in this study were mainly obtained from the deployment of 12 BBOBSs [*Shiobara et al.*, 2000] in the Philippine Sea region from October 2005 to November 2006 as part of the Stagnant Slab Project [*Fukao et al.*, 2009]. The sites were equipped with three-component Guralp CMG-3T sensors (24-bit recording, 200 Hz sampling). We also consider waveform data from the land station OSW (on the Ogasawara islands), part of the Japanese F-net broadband seismograph network. Summary information on all of the stations used in this study is provided in Figure 1 and Table 1. We analyze local earthquakes (epicentral distance <12°) that sample the Izu-Bonin slab and surrounding mantle (i.e., both above and beneath the slab). The locations of the seismic events and stations are shown in Figure 1. All events were located in the Izu-Bonin subduction zone at 23°–33°N, 135°–145°E, and 100–500 km depth, with event magnitudes (m_b) of $4.7 < m_b < 5.9$. We consider 10 events that provide adequate signal-to-noise ratios (Figure 1 and Table 2). Although the stations have variable recording periods, all record data for at least 1 event.

3. Attenuation Measurements

[8] Attenuation is measured on the basis of the high-frequency decay of P waves. The amplitude spectra as a function of frequency f can be expressed by

$$A(f) = CA_S(f)A_I(f)A_Q(f), \tag{1}$$

where $A_S(f)$ is the source spectrum, $A_I(f)$ is the instrumental response, $A_Q(f)$ is the attenuation, and C is a constant that takes into account the frequency-independent radiation pattern and geometric spreading effects. C may also include frequency-independent site amplification. The amplitude decay with frequency due to attenuation is expressed as

$$A_Q(f) = \exp\left[-\pi f \int dt/Q(f)\right], \tag{2}$$

where $Q(f)$ is the frequency-dependent seismic attenuation quality factor and dt is the incremental traveltime. On the basis of previous experimental [*Jackson*, 2000] and seismological [*Roth et al.*, 1999; *Shito et al.*, 2004; *Stachnik et al.*, 2004] studies, we assume that $Q(f)$ has a power law frequency dependence:

$$Q(f)^{-1} = Q_0^{-1}(f/f_0)^{-\alpha}, \tag{3}$$

Table 1. Summary Information for the Stations Used in this Study

Code	Network	Latitude (°N)	Longitude (°E)	Elevation (m)	Period	Sensor
T06	SSP	29.9889	134.9751	−4614	6 Oct. 2005 to 30 Oct. 2006	CMG-3T
T07	SSP	27.9001	135.9218	−5259	7 Oct. 2005 to 16 Nov. 2005	CMG-3T
T08	SSP	25.7680	137.0075	−4894	7 Oct. 2005 to 16 Jul. 2006	CMG-3T
T09	SSP	30.6683	137.3235	−4260	6 Oct. 2005 to 30 Oct. 2006	CMG-3T
T11[a]	SSP	22.6698	137.9841	−4770	17 Oct. 2005 to 8 Nov. 2006	CMG-3T
T12	SSP	27.4997	138.5126	−4679	21 Oct. 2005 to 11 Nov. 2006	CMG-3T
T13	SSP	24.9739	139.2976	−4786	22 Oct. 2005 to 17 Nov. 2005	CMG-3T
T15	SSP	28.9991	141.3211	−4020	21 Oct. 2005 to 16 Nov. 2006	CMG-3T
T17	SSP	29.3265	145.3329	−5794	20 Oct. 2005 to 17 Nov. 2006	CMG-3T
T18	SSP	27.1419	147.1735	−5582	20 Oct. 2005 to 15 Nov. 2006	CMG-3T
T19	SSP	23.9927	148.0087	−5772	18 Oct. 2005 to 13 Nov. 2006	CMG-3T
T21	SSP	27.3079	150.6005	−5858	19 Oct. 2005 to 6 Mar. 2006	CMG-3T
OSW	F-net	27.0983	142.1961	11	2 Mar. 2002 to present	STS-2

[a]T11 only has vertical component data.

Table 2. Summary Information for the Events Used in This Study

Date	Latitude (°N)	Longitude (°E)	Depth (km)	Magnitude
27 Oct. 2005	30.87	138.47	382	5.2 M_w
27 Nov. 2005	27.04	140.26	442	4.7 m_b
2 Dec. 2005	25.05	141.62	521	5.0 M_w
29 Dec. 2005	27.37	139.85	472	5.3 M_w
3 Jan. 2006	29.15	139.34	415	4.7 m_b
17 Feb. 2006	24.02	141.49	160	5.6 M_w
28 Mar. 2006	31.71	137.75	401	5.9 M_w
3 Apr. 2006	30.82	140.19	119	4.9 m_b
16 Apr. 2006	30.24	138.57	431	5.7 M_w
26 May 2006	30.40	138.35	438	4.9 m_b

where Q_0^{-1} is the attenuation at the reference frequency f_0. We use f_0 = 1.0 Hz in this study. We introduce an attenuation operator that describes the path-integrated attenuation

$$t_0^* = \int dt/Q_0. \tag{4}$$

On the basis of equations (3) and (4), equation (2) becomes

$$A_Q(f) = \exp\left[-\pi f t_0^* (f/f_0)^{-\alpha}\right]. \tag{5}$$

The instrument response $A_I(f)$ is known and removed. We also remove the source spectrum $A_S(f)$, which is estimated using methods introduced in the following section. After the corrections, the spectra can be expressed as

$$A(f) = C\exp\left[-\pi f t_0^* (f/f_0)^{-\alpha}\right]. \tag{6}$$

Taking the natural logarithm of both sides of equation (6), we obtain

$$\ln[A(f)] = C - \pi f t_0^* (f/f_0)^{-\alpha}. \tag{7}$$

t^*_0 is hereafter referred to as t^*, without the subscript "0."

[9] A grid search method is applied to determine the best fit value of the attenuation operator t^* in the parameterized model of equation (7) for the corrected spectra. Figures 2a and 2b illustrate the process employed in calculating the spectral ratio curve. The P wave is taken from the vertical component (Figure 2a). We manually pick the P wave arrival after applying a band-pass filter at 0.5–9.5 Hz and resampling at 20 Hz. The arrival is then windowed from 2.5 s before the onset of the P wave to 12.5 s after. The time window is long enough to include all the energy from the P wave. This attenuation measurement possibly includes a contribution from scattering; however, the observed simple waveforms without prominent coda (Figure 2a) indicate that intrinsic attenuation is vastly more dominant than scattering attenuation. Also shown in the Figure 2a is a sample of noise taken from the time window between 25 and 5 s before P wave arrival. A fast Fourier transform is applied to the 10% cosine tapered waveforms to calculate the amplitude spectra. Figure 2b shows the natural log spectra smoothed using a Hanning window with a bandwidth of 0.06 Hz. A sample of the noise spectra is also shown as an indication of data quality, showing a high signal-to-noise

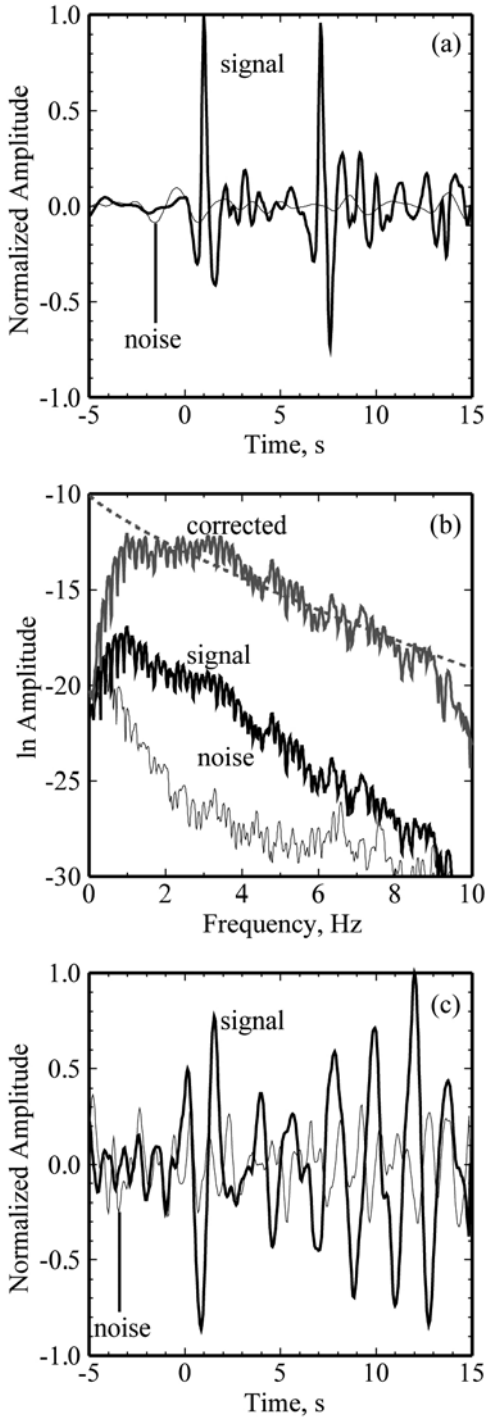

Figure 2. (a) Typical time domain waveform of a P wave recorded at a BBOBS station (T06) located within the Philippine Sea (vertical component). The hypocenter is located at 472 km depth in the Izu-Bonin slab. Thick and thin lines indicate signal and noise, respectively. (b) Natural log amplitude spectra of the P waveforms. Thick and thin black lines show the signal and noise spectra, respectively. The gray line is the corrected spectra, and the dashed line is the fitted curve. (c) Typical time domain waveform of the S wave (transverse component). The events and stations are the same as those for the P wave.

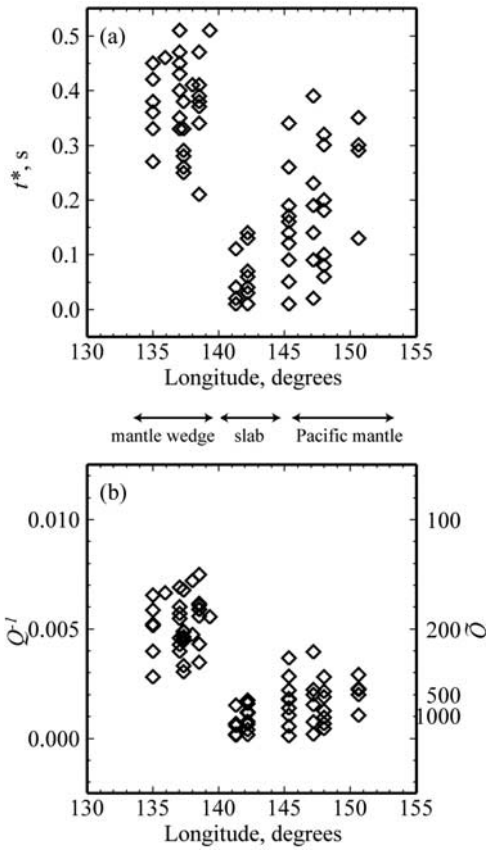

Figure 3. (a) Path-integrated attenuation t^* plotted versus station longitude. (b) Path-averaged attenuation Q^{-1} plotted versus station longitude. Note that t^* and Q^{-1} are estimates of P wave attenuation.

ratio. A frequency band of 1.0–9.0 Hz (excluding 5.0–7.0 Hz) is used in estimating t^*. This range is determined by taking into account the signal-to-noise ratio. In some BBOBS data, the characteristic noise is found at 5.0–7.0 Hz. The energy level shows irregular rises and falls in both space and time. The noise is possibly vertically polarized shear waves, which are efficiently coupled with compressional waves at the seafloor [*Webb*, 1998]. Because the source of the noise is not the primary focus of this study, we simply exclude this frequency range from the analysis.

[10] The spectra corrected for the source and instrumental response are shown by the gray line in Figure 2b. For each spectrum, we searched for the optimum t^* and C in equation (7). The grid spacing is $\Delta t^* = 0.001$ s from 0.000 to 1.000 s and $\Delta C = 1.0$ from -50.0 to 50.0, a wide enough range to cover all possible values. The typical error in the fitting parameter t^* is 0.0035 s. The value of C only controls the absolute level of the amplitude spectra, which does not influence the attenuation measurement. The frequency-dependent Q^{-1} model defined by equation (7) with $\alpha > 0$ yields less attenuation at high frequencies relative to a constant Q^{-1} model ($\alpha = 0$), resulting in a concave upward spectra (Figure 2b). This curvature is dominant, especially at low frequencies of $f < 1$ Hz, which we do not use in this study. Therefore, the value of α is not critical in this fitting process. In this study we use $\alpha = 0.2$, as estimated in a previous study [*Shito et al.*, 2004].

[11] All the spectra with high signal-to-noise ratios are well fitted, yielding 82 estimates of t^* (see Figure 3a). The values of t^* show a systematic trend with station longitude in spite of a wide variation depending on the location and length of the raypath. From the path-integrated attenuation t^*, the path-averaged attenuation is obtained by $Q^{-1} = t^*/t$, as shown in Figure 3b, which clearly shows the systematic trend with longitude. Data recorded at stations in the Philippine Sea (longitude < 140°E; T06, T07, T08, T09, T11, T12, and T13) that sample the mantle wedge above the Izu-Bonin slab show $Q = \sim 150-300$ (high attenuation). Data recorded at stations located close to the trench (140°E < longitude < 145°E; T15 and OSW) that mainly sample the slab give $Q = \sim 500-1000$ (low attenuation). Data recorded at stations located in the Pacific Ocean (longitude > 145°E; T17, T18, T19, and T21) that sample the Pacific mantle beneath the slab show a wide range in Q values (250–1000; low to moderate attenuation) depending on the distance from the slab. Because higher values of Q are obtained for raypaths located closer to the slab, some raypaths are considered to graze the lower edge of the slab. Those raypaths corresponding to $Q < 200$, $200 < Q < 500$, and $Q > 500$ are shown separately in Figure 4, demonstrating systematic differences in Q in different regions.

4. Source Models

[12] The following two methods are used to estimate the source spectra $A_S(f)$ for each event, which are then removed from the observed spectra.

4.1. The ω^2 Model

[13] We assume a simple ω^2 source spectrum [*Houston and Kanamori*, 1986]

$$A_S(f) = A_S(f_c) / \left[1 + (f/f_c)^2\right]. \tag{8}$$

Taking the natural logarithm of both sides of equation (8), we obtain

$$\ln[A_S(f)] = C - \ln\left[1 + (f/f_c)^2\right]. \tag{9}$$

The corner frequency f_c is given by the following relation [*Houston and Kanamori*, 1986]:

$$f_c = 0.49\beta[\Delta\sigma/M_o]^{1/3}, \tag{10}$$

where M_o is the seismic moment, β is the S wave velocity in the source area (as taken from the one-dimensional reference model ak135 [*Kennett et al.*, 1995] depending on the source depth) and $\Delta\sigma$ is the stress drop. We use $\Delta\sigma = 30$ MPa, which is a typical value for deep focus earthquakes [*Venkataraman and Kanamori*, 2004]. The estimated values of f_c vary from 0.10 to 0.32 Hz, depending on the seismic moment and source depth.

4.2. Slab Station Model

[14] Waveform data recorded at a land station located just above the trench (OSW in Figure 1) mainly sample the slab. The high-frequency components of the waveform indicate a minor attenuation effect (Figure 5a). Therefore, the spectra

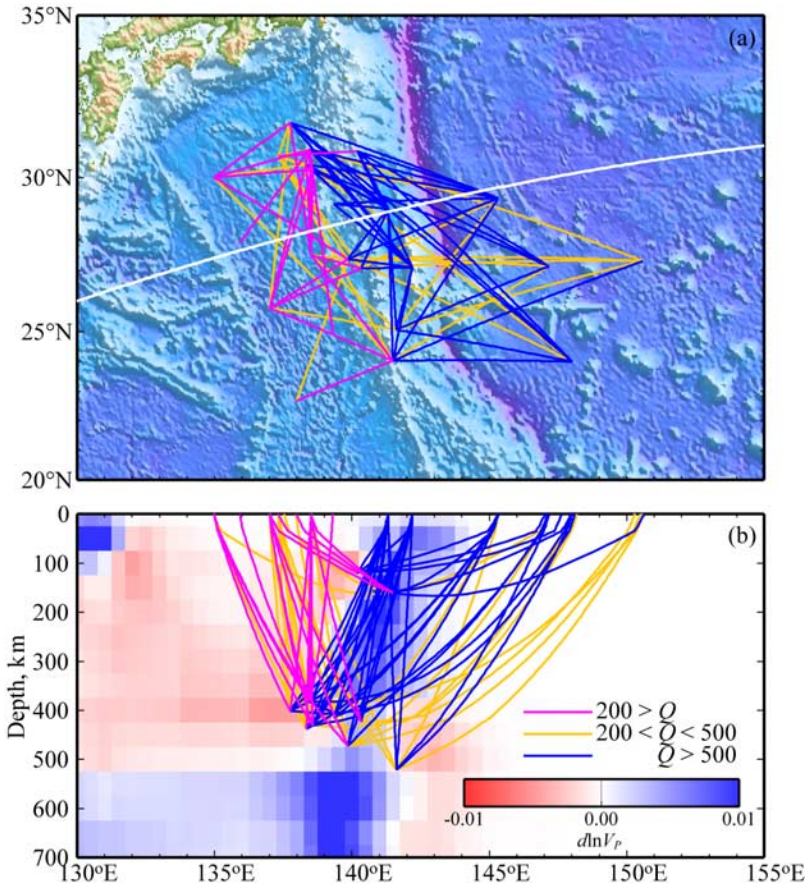

Figure 4. (a) P wave raypaths classified into three groups according to the path-averaged attenuation Q^{-1}. Bathymetric data are from ETOPO5 (NOAA National Geophysical Data Center). (b) Cross section along the longest line shown in Figure 4a. Background color indicates P wave velocity structure [*Gorbatov and Kennett*, 2003].

of this station corrected for the instrument response $A_I(f)$ can be assumed to give the source spectra $A_S(f)$ (Figure 5b). Figure 5c shows t^* obtained using the source spectra estimated from the slab station model t^*(OSW) versus t^* obtained using the source spectra estimated from the ω^2 model $t^*(\omega^2)$. Estimated values of $t^*(\omega^2)$ and t^*(OSW) are generally consistent, demonstrating the robustness of the two methods; however, when assessed in detail, t^*(OSW) values are systematically smaller than $t^*(\omega^2)$ values by about 0.05 s, reflecting the fact that the source spectra estimated using the slab station model are slightly smaller than the actual source spectra due to a small but non-negligible attenuation in the slab. Therefore, we use $t^*(\omega^2)$ in the following analysis.

5. Traveltime Residual

[15] At the same time as conducting attenuation measurements, we measure the traveltimes of 82 P waves and 68 S waves. We visually pick P wave arrivals from the vertical component (Figure 2a) and S wave arrivals from the transverse component (Figure 2c). Because the signal-to-noise ratio of S wave data is lower than that of P wave data, we consider fewer S wave traveltimes (we make no estimates of S wave attenuation). We calculate the traveltime anomaly $d\ln t$, which is equal to the velocity anomaly $d\ln V$, although with the opposite sign:

$$d\ln t = (t - t_r)/t = -(V - V_r)/V_r = -d\ln V, \qquad (11)$$

where the subscript r indicates values calculated for the reference model. The theoretical traveltime t_r is calculated using the reference velocity model ak135 and source information provided in a catalog of Preliminary Determinations of Epicenters (PDE) located by U.S. Geological Survey.

[16] The calculated traveltime anomalies are shown in Figure 6. Considering errors in hypocenter location and traveltime picking, we roughly estimate uncertainties in the P and Swave traveltime anomalies. The typical error in source time reported in the catalog of Earthquake Data Report (EDR) is 0.2 s. On the basis of the quality of traveltime picking, we define uncertainties in P and S wave traveltimes to be 0.5 and 1.0 s, respectively (see Figures 2a and 2c). The S wave traveltimes are less accurate than the P wave traveltimes because of the low signal-to-noise ratio. Considering the total error in P and S wave traveltime residuals (0.7 and 1.2 s for P and S waves, respectively) and

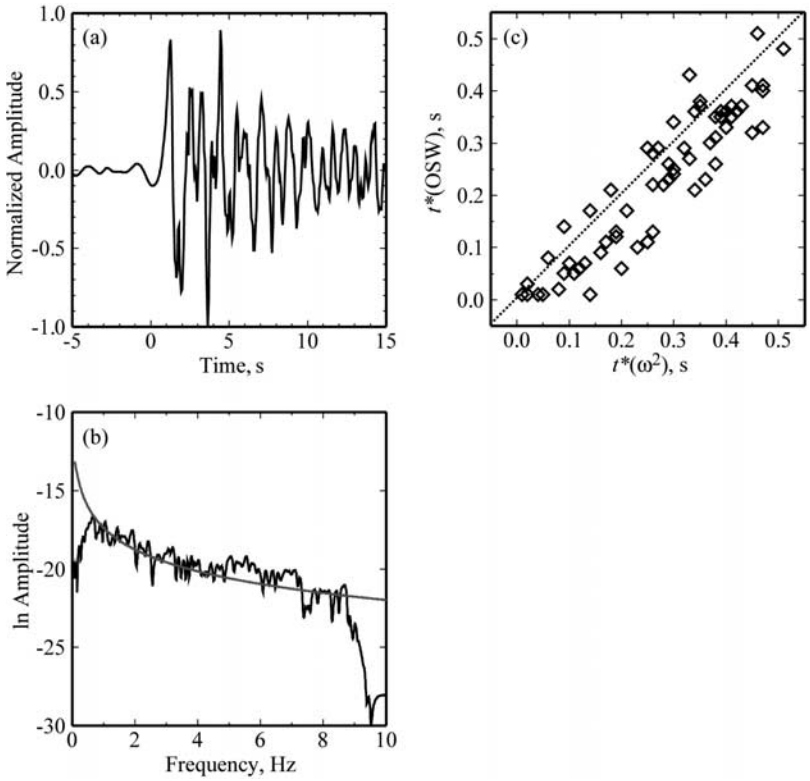

Figure 5. (a) Typical time domain waveform of a P wave recorded at a land station (OSW) located on Ogasawara Island. (b) Natural log amplitude spectra of the waveform. Gray line indicates the source spectra estimated from the ω^2 model. The spectra observed at the slab station is similar to the synthetic spectra estimated from the ω^2 model. (c) Comparison of t^* estimated using the ω^2 model and the slab station model.

typical traveltimes (65 and 120 s for P and S waves, respectively), the uncertainty in traveltime anomalies is 0.01 for both P and S waves. Although the variance of the calculated traveltime anomaly is large, several systematic trends are common to both P and S waves. Most mantle wedge data have $0.02 < d\ln t_{P,S} < 0.05$ (positive anomaly), most slab data yield $-0.07 < d\ln t_{P,S} < -0.01$ (negative anomaly), and the Pacific mantle data give $-0.05 < d\ln t_{P,S} < 0.00$ (from a negative anomaly to no anomaly) depending on distance from the slab. The magnitudes of the P wave traveltime anomalies are similar to those for S waves. The intensities of the traveltime anomalies are 2–3 times larger than those of the velocity perturbation in tomographic models obtained previously near our target area [*Gorbatov and Kennett*, 2003]. Our data set based on local events obtained by BBOBS deployment provide better path coverage and resolution, and hence more accurate velocity estimates, than those obtained in the previous tomographic study, which used only teleseismic data obtained by land stations. In addition, estimates of absolute velocity based on tomographic models may be biased by factors such as the choice of damping parameters and initial model.

6. Attenuation and Velocity Anomalies

[17] A quantitative comparison of seismic attenuation and velocity provides useful information on the physical properties of the Earth's interior. The relation between Q^{-1} and $d\ln t$ for P waves is shown in Figure 7, in which the symbols represent observed data and lines show the relation between attenuation and traveltime anomaly due to the thermal effect for three representative depths (0, 100, and 400 km). These lines are calculated theoretically on the basis of equations (12) and (13) below. Attenuation is given as a function of temperature T

$$Q^{-1} = Cf^{-\alpha}\exp[-\alpha H^*/RT], \tag{12}$$

where H^* is the activation enthalpy, R is the gas constant, and C is a constant [*Kampfmann and Berckhemer*, 1985]. The velocity anomaly due to the thermal effect consists of an anharmonic effect and an anelastic effect

$$d\ln V = (\partial \ln V/\partial T)_{\mathrm{anh}} dT - 1/2\cot(\pi\alpha/2)\left(Q^{-1} - Q_r^{-1}\right), \tag{13}$$

where dT is the temperature difference relative to the reference temperature ($dT = T - T_r$) [*Karato*, 1993]. The values of the parameters used in equations (12) and (13) are summarized in Table 3. The anharmonic effect $(\partial \ln V/\partial T)_{\mathrm{anh}}$ is calculated for a pyrolite composition on the basis of finite strain theory [*Duffy and Anderson*, 1989] and an experimental database [*Ita and Stixrude*, 1992]. The reference temperature T_r is calculated for an oceanic geotherm of 50 Ma in age. Q_r^{-1} is the reference attenuation, taken from the preliminary reference Earth model (PREM) [*Dziewonski and Anderson*, 1981]. The constant C is calculated by

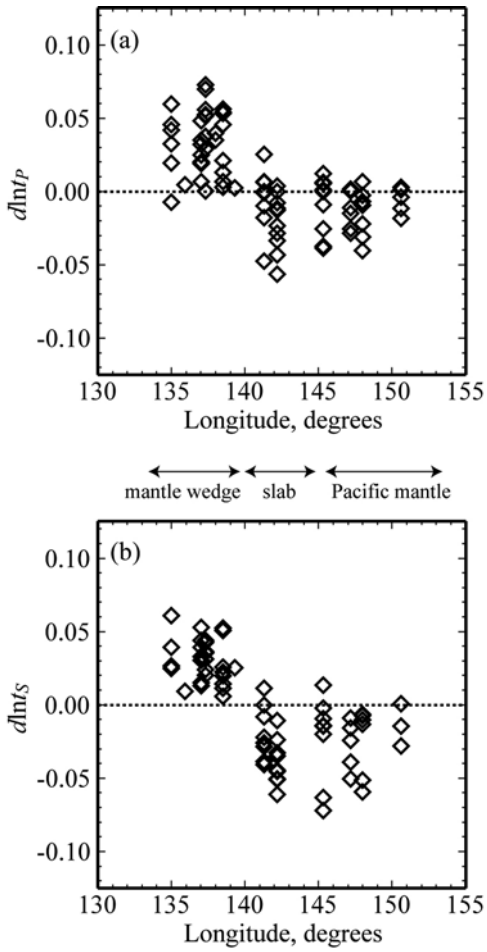

Figure 6. (a) P wave traveltime anomalies $d\ln t_P$ plotted versus station longitude. (b) S wave traveltime anomalies $d\ln t_S$ plotted versus station longitude.

substituting Q_r^{-1} and T_r into equation (12). Using equations (12) and (13), the theoretical relation between Q^{-1} and $d\ln t$($= -d\ln V$) is calculated for the temperature range of -500 K $< dT <$ 500 K. The relations between Q^{-1} and $d\ln t$ at depths greater than 200 km are similar to that at 400 km depth. Both the slab data and Pacific mantle data generally follow the predicted curves on the basis of the thermal effect. In contrast, the mantle wedge data show considerably more intense positive traveltime anomalies than those predicted from the attenuation. These anomalies are difficult to explain solely in terms of the thermal effect.

[18] Partial melt affects velocity and attenuation via the poroelastic effect and enhanced grain boundary sliding. Theoretical studies show that the low-velocity anomaly caused by the poroelastic effect is not accompanied by high attenuation, as the timescale of melt squirt flow is much shorter than the periods of seismic waves [*Faul et al.*, 2004; *Hammond and Humphreys*, 2000a, 2000b]. The present seismological observations are explained by the relation between velocity anomaly and attenuation predicted for the poroelastic effect. The effect of melt on grain boundary sliding is poorly understood. Experimental data obtained at seismic frequencies show that the effects can be significant [*Faul et al.*, 2004; *Jackson et al.*, 2004]; however, there exist few theoretical models, and uncertainties exist in extrapolating experimental data obtained at small grain sizes to mantle conditions. In addition, enhanced grain boundary sliding dominantly affects $d\ln V_S$, making it difficult to explain the relatively large amplitude of $d\ln V_P$, which is comparable to the $d\ln V_S$ anomalies described below. Therefore, only the poroelastic effect is considered in our analysis of the effects of partial melt on velocity and attenuation.

[19] Figure 8 shows the relation between $d\ln t_P$ and $d\ln t_S$. The predicted lines are obtained from equations (12) and (13) using the parameters listed in Table 3. Again, the slab data and the Pacific mantle data are consistent with predictions, with the mantle wedge data deviating slightly from the predicted curves.

7. Discussion

7.1. Temperature Anomalies

[20] As mentioned above, by considering that the attenuation is insensitive to partial melt and primarily reflects the thermal effect, we can estimate the temperature anomaly dT from observed Q^{-1} via equation (12). The path-averaged temperature anomalies inferred from the path-averaged attenuation are shown in Figure 9. The temperature anomalies in the mantle wedge range from +100 to +250 K, while the temperature anomalies in the slab range from -100 to -500 K. The temperature anomalies in the Pacific mantle vary from -400 to 0 K depending on distance from the slab. The relative temperature anomalies are generally consistent with the results of a previous numerical simulation [*Yoshioka and Sanshadokoro*, 2002]. The maximum temperature anomaly in the mantle wedge is about +250 K. If we assume that the area of high attenuation is restricted to depths of 50–150 km, the maximum temperature anomaly is then > +300 K. In both cases ($dT = \sim$+250 K and $dT >$ +300 K) the absolute temperature $T = T_r + dT$ exceeds the dry solidus of mantle peridotite at depths of 75–100 and 75–125 km, respectively (Figure 10). This result suggests the existence of partial melt.

7.2. Partial Melt

[21] Following the method introduced by *Nakajima et al.* [2005], we corrected for the traveltime anomalies due to the thermal effect, as estimated by substituting dT (Figure 9) into equation (13). The anomalies are much smaller than the total traveltime anomalies (Figure 11a). The residual traveltime anomalies (defined as total traveltime anomalies minus the traveltime anomalies due to the thermal effect) are considered to reflect the existence of partial melt (Figure 11b). We note that the data recorded at station T09 have systematically pronounced traveltime anomalies (see Figure 11), perhaps related to the fact that this station is located closest to the trench and active volcanoes (e.g., Hachijojima and Aogashima), as shown in Figure 1.

[22] The slope of $d\ln t_S$ plotted versus $d\ln t_P$ is equal to the relative magnitude of S to P wave velocity anomaly

$$R_{S/P} = d\ln V_S / d\ln V_P = -d\ln t_S / -d\ln t_P. \qquad (14)$$

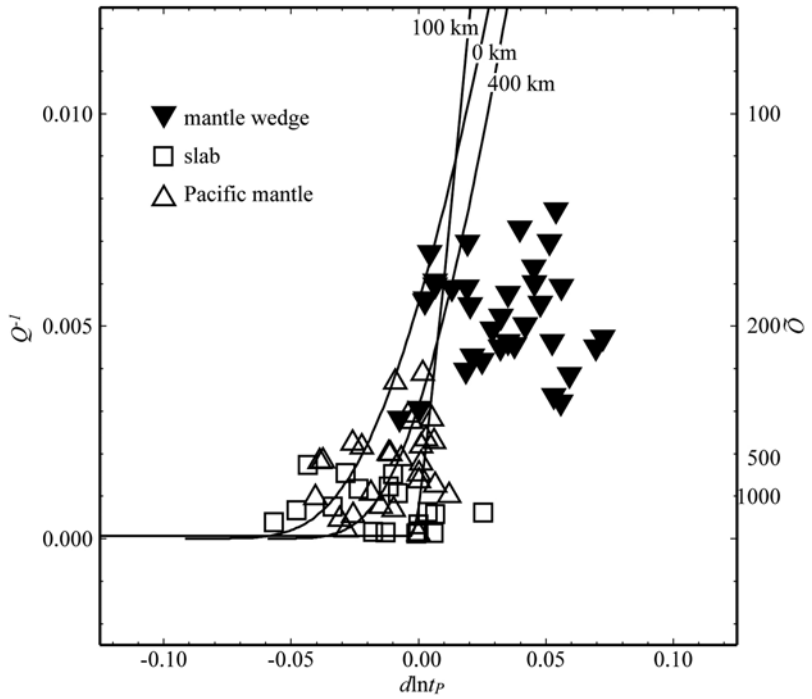

Figure 7. Relation between the path-averaged attenuation Q^{-1} and traveltime anomalies $d\ln t_P$. Symbols represent observed data. Lines are predictions based on the thermal effect for various depths (0, 100, and 400 km). Note that Q^{-1} values are estimates of P wave attenuation.

$R_{S/P}$, commonly used as a parameter to infer the origin of seismic velocity anomalies, is estimated by computing the slope of the fitting line in a plot of $d\ln t_S$ versus $d\ln t_P$. The best fit line is calculated to minimize the sum of distances between data points and the line, with the distances being measured perpendicular to the line. In the fitting process, we take on the constraint that the line intercepts the origin on the basis of the assumption that the traveltime anomalies are mostly caused by temperature anomalies and presence of partial melt, for which changes in P and S wave velocities have the same sign. The value of $R_{S/P}$ estimated from 26 traveltime anomalies within the mantle wedge is 0.93 without correction for the thermal effect (Figure 11a), and 0.64 with correction (Figure 11b). These values are smaller than that corresponding to the thermal effect ($R_{S/P} = 1.38$). Previous theoretical and experimental studies show that the value of $R_{S/P}$ corresponding to texturally equilibrated partial melt is $1.0 < R_{S/P} < 1.5$ [*Takei*, 2002; *Yoshino et al.*, 2005]. Therefore, the finding of a $R_{S/P}$ value smaller than the thermal effect can be explained by the existence of a texturally equilibrated partial melt. In some cases, the existence of partial melt would result in lower $R_{S/P}$ values; however, the values obtained as the slopes of the fitting lines are lower than 1.0, and further analysis based on the assumption of partial melt is difficult.

[23] We calculate the values of $R_{S/P} = -d\ln t_S/d\ln t_P$ for each data point in Figure 11b; the values are shown in Figure 12 (diamonds on the right-hand edge). In terms of the reliability of the data, values of $R_{S/P}$ are generally in the range 0.5–1.2. Compared with thin dikes or cracks ($R_{S/P} > 2$), the obtained $R_{S/P}$ values are better explained by textually equilibrated melt or aqueous fluid. We also estimate the effective aspect ratio γ and volume fraction ϕ of melt-filled pores from $R_{S/P}$ and $d\ln t_S$ following the method proposed by *Takei* [2002] (Figure 12). This method is based on the results of theoretical studies of the effects of pore fluid compressibility, pore geometry (represented by effective aspect ratio γ), and melt fraction on $d\ln V_P$ and $d\ln V_S$. If the fluid compressibility normalized to that of the host rock, $\kappa_f^{-1}/\kappa_s^{-1}$, is given, we can estimate γ from the value of $R_{S/P}$. Once γ is obtained, ϕ can be estimated from $d\ln t_S$. We use $\kappa_f^{-1}/\kappa_s^{-1} = 7$ in this study. If we use $R_{S/P} = 1.2$, we obtain $\gamma = 0.1$, which corresponds to the values for textually equilibrated partially molten rock. With $\gamma = 0.1$, the partial

Table 3. Values of Parameters Used in Equations (12) and (13)

Depth (km)	T_r[a] (K)	Q_{Pr}[b]	Q_{Sr}[b]	H^*[c] (kJ/mol)	C	$(d\ln V_P/dT)_{anh}$[d] (10^{-5}K^{-1})	$(d\ln V_S/dT)_{anh}$[d] (10^{-5}K^{-1})
0	300	1350	600	420	3.18×10^{11}	8.97	8.49
100	1571	180	80	463	6.68	8.31	8.31
400	1800	366	143	605	10.13	5.43	6.27

[a]Oceanic geotherm of 50 Ma in age calculated on the basis of a cooling model [*Turcotte and Schubert*, 1982].
[b]Taken from PREM [*Dziewonski and Anderson*, 1981].
[c]Calculated using the pressure dependence of the activation volume [*Kampfmann and Berckhemer*, 1985].
[d]Calculated on the basis of finite strain theory [*Duffy and Anderson*, 1989] and mineralogical data [*Ita and Stixrude*, 1992].

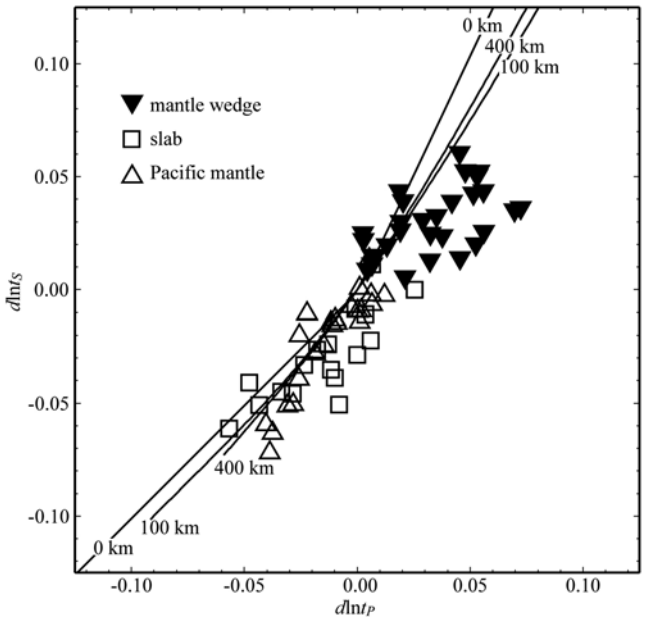

Figure 8. Relation between P wave traveltime anomalies $d\ln t_P$ and S wave traveltime anomalies $d\ln t_S$. Symbols represent observed data. Lines are predictions based on the thermal effect for various depths (0, 100, and 400 km).

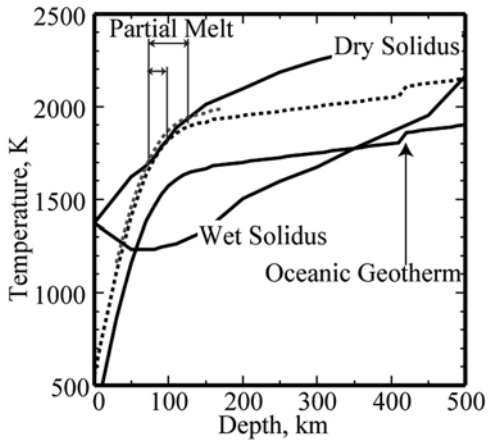

Figure 10. Comparison of temperature in a typical mantle wedge with the solidus curve for peridotite. The oceanic geotherm of 50 Ma in age, corresponding to the reference temperature T_r, is calculated using a simple cooling model of the oceanic lithosphere [*Turcotte and Schubert*, 1982]. The dry and wet (1–2 wt % H_2O) solidus curves shallower and deeper than 125 km are taken from experimental results for peridotite [*Kushiro*, 2007] and CaO–MgO–Al2O3–SiO2-pyrolite [*Litasov and Ohtani*, 2002], respectively. Black and gray dashed lines indicate the temperature anomalies of +250 and +300 K, respectively, which exceed the dry solidus of peridotite at depths of 75–100 and 75–125 km, respectively.

derivative $-d\ln V_S/d\phi$ is determined to be 2.0 (Figure 12). If we assume $-d\ln V_S/d\phi = 2.0$ for all data, the melt fraction ϕ is estimated to be $\phi = \sim 0.0–2.5\%$ from $d\ln t_S = \sim 0.0–0.05$ (Figure 11b).

[24] It is difficult to explain small values of $R_{S/P}$ (i.e., < 1.0) in terms of partial melt. Such values remain small over the uncertainty range expected from errors in traveltime residuals. Similar difficulties were also reported by *Nakajima et al.* [2005], as discussed below. One possible explanation of such small $R_{S/P}$ values is the existence of aqueous fluids within pores with large aspect ratios (Figure 12). Another explanation of low-velocity anomalies may be compositional heterogeneity in the host rock; however, it is difficult to explain the pronounced low-velocity anomalies obtained in the present study solely in terms of the effect of compositional changes in the host rock resulting from partial melt [*Matsukage et al.*, 2005].

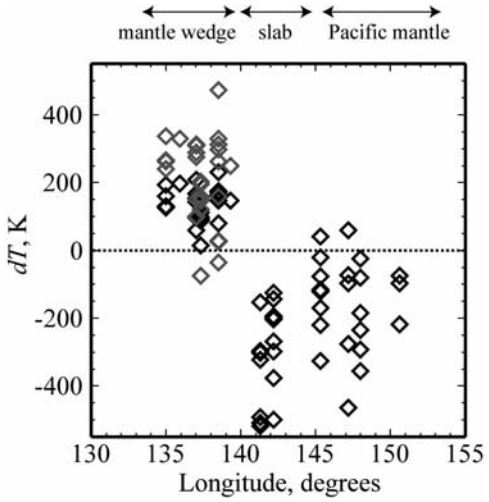

Figure 9. Temperature anomalies dT plotted versus station longitude. Black symbols indicate estimates based on the assumption that the temperature anomalies are constant along the raypaths. Gray symbols represent estimates based on the assumption that the high attenuation in the mantle wedge is limited to depths of 50–150 km.

[25] The difficulty involved in interpreting such small $R_{S/P}$ values may arise from the effect of anisotropy. In this study, we do not consider the possibility of anisotropy in our data analysis or interpretation; however, *Anglin and Fouch* [2005] reported seismic anisotropy in this region. The shear wave splitting times for local S waves range from 0.6 to 1.7 s, and the fast polarization direction is nearly parallel to the trench [*Anglin and Fouch*, 2005]. Therefore, the traveltime residual observed in this study may also be subject to the anisotropy. Because the diagram shown in Figure 12 assumes an isotropic structure consisting of randomly oriented pores, the difficulty in explaining the observed values of $R_{S/P}$ based on Figure 12 may indicate the existence of strongly oriented melt pores. Further refinements are required in data analysis and theoretical modeling by taking into account the effect of anisotropy. The upcoming results of an electromagnetic survey performed in the present study region as part of the Stagnant Slab Project will provide further constraints on the possible existence of melt or aqueous fluid.

7.3. Comparison With Previous Studies

[26] In a study of the Tonga subduction zone, *Roth et al.* [2000] obtained an empirical relation between attenuation

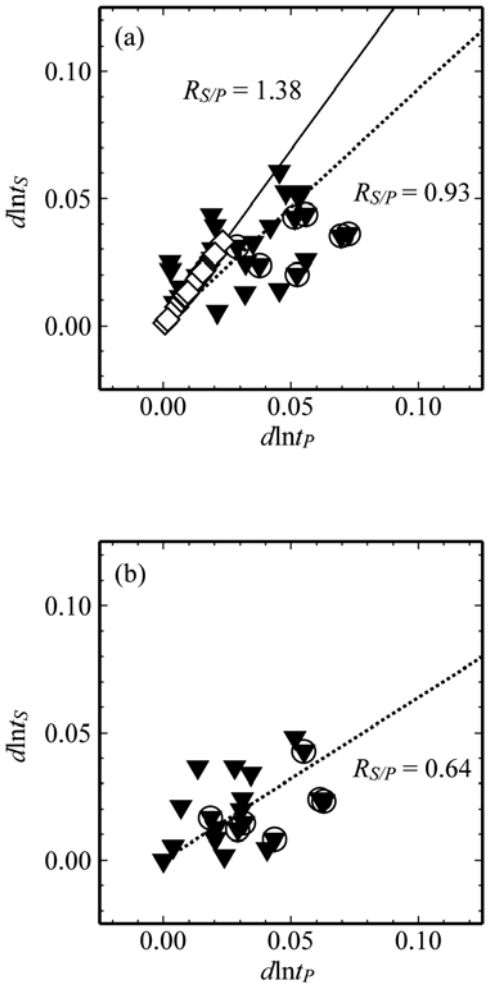

Figure 11. (a) Relation between P and S wave traveltime anomalies in the mantle wedge. Triangles indicate total traveltime anomalies. Circled triangles represent data from station T09. Diamonds indicate traveltime anomalies due to the thermal effect. The dashed line is the regression line for the plot of total traveltime anomalies (slope is 0.93). The solid line is the regression line for the plot of traveltime anomalies due to the thermal effect (slope is 1.38). (b) Residual traveltime anomalies (defined as total traveltime anomalies minus traveltime anomalies due to the thermal effect), which may indicate the traveltime anomaly due to partial melt. The dashed line is the regression line for the plot (slope is 0.64).

and velocity using tomographic models [*Roth et al.*, 1999; *Zhao et al.*, 1997]. This relation is generally consistent with the effect of temperature, except at shallow depths (0–100 km), which show pronounced low-velocity anomalies compared with the attenuation anomalies. The authors suggested that the presence of partial melt may produce such pronounced low-velocity anomalies, which are much more intense than would be expected from the temperature effect. The data of *Roth et al.* [2000] are plotted in Figure 13a. Each pair of Q^{-1} and $d\ln t$ values for each symbol in Figure 13a are taken from the same spatial location in the velocity and attenuation tomographic models. Similar to our results for the Izu-Bonin region, the data of *Roth et al.* [2000] show pronounced low-velocity anomalies compared with the attenuation.

[27] *Koper et al.* [1999] used traveltime measurements to examine $R_{S/P}$ in the Tonga subduction zone. For the mantle wedge, they obtained values of $1.2 < R_{S/P} < 1.3$ (without correction for the thermal effect). The authors noted that the relatively small value of $R_{S/P}$ is inconsistent with previous estimates of $R_{S/P}$ for partial melt (e.g., $1.8 < R_{S/P} < 2.3$ [*Faul et al.*, 1994]), and suggested that previous theoretical studies may have overestimated $R_{S/P}$ for partial melt. *Faul et al.* [1994] estimated $R_{S/P}$ based on an oblate spheroid model; however, their method of approximating the complex geometry of melt by a simple oblate spheroid is without a solid theoretical foundation. *Yoshino et al.* [2005] estimated $R_{S/P}$ based on a granular model, in which geometrical parameter contiguity is measurable from microstructural observations of the partially molten rocks. The value of $R_{S/P}$ estimated by *Yoshino et al.* [2005] is much smaller ($1.0 < R_{S/P} < 1.5$) than that estimated by *Faul et al.* [1994], indicating that the pore aspect ratio corresponding to textually equilibrated partially molten rock is larger than that estimated by *Faul et al.* [1994].

[28] For the Tohoku subduction zone, we compared the attenuation and velocity of P waves taken from tomographic models [*Nakajima et al.*, 2001; *Tsumura et al.*, 2000]. Again, as with our result for the Izu-Bonin subduction zone, the tomography data show a pronounced low-velocity anomaly without comparable high attenuation (Figure 13b). *Nakajima et al.* [2005] estimated $0.6 < R_{S/P} < 1.3$ (after correction for the thermal effect) at 90 km depth based on a velocity tomography by *Nakajima et al.* [2001]. They estimated volume fraction of partial melt of 3–6%. Their results are similar to our findings for the Izu-Bonin subduction zone. The authors reported much larger values of $R_{S/P}$ ($1.5 < R_{S/P} < 2.5$) at shallower depths (40 and 65 km), thereby interpreting the existence of melt in thin cracks or as dikes.

[29] Figure 14 summarizes the results of studies on the Tonga [*Koper et al.*, 1999; *Roth et al.*, 2000], Tohoku [*Nakajima et al.*, 2005], and Izu-Bonin subduction zones (this study). All of these studies document pronounced low-velocity anomalies unaccompanied by comparable high attenuation, and relatively small $R_{S/P}$ (<1.5). Small values of $R_{S/P}$ (<1.5) are consistent with theoretical and experimental studies of textually equilibrated partial melt. We therefore emphasize that the existence of partial melt does not always result in large values of $R_{S/P}$ (>1.5).

8. Conclusions

[30] On the basis of BBOBS waveform data, we estimate seismic attenuation and traveltime anomalies in the vicinity of the Izu-Bonin subduction zone. We analyzed data from regional (<12°) earthquakes that sample the mantle wedge above the slab, the slab itself, and the Pacific mantle beneath the slab, and measured 82 path-averaged attenuation and traveltime anomalies of P waves and 68 traveltime anomalies of S waves. The observed attenuation and traveltime anomalies vary systematically across the trench. The mantle wedge data show high attenuation ($Q_P = \sim 150–300$) and positive traveltime anomalies ($0.02 < d\ln t_{P,S} < 0.05$), whereas the slab data yield low attenuation ($Q_P = \sim 500–$

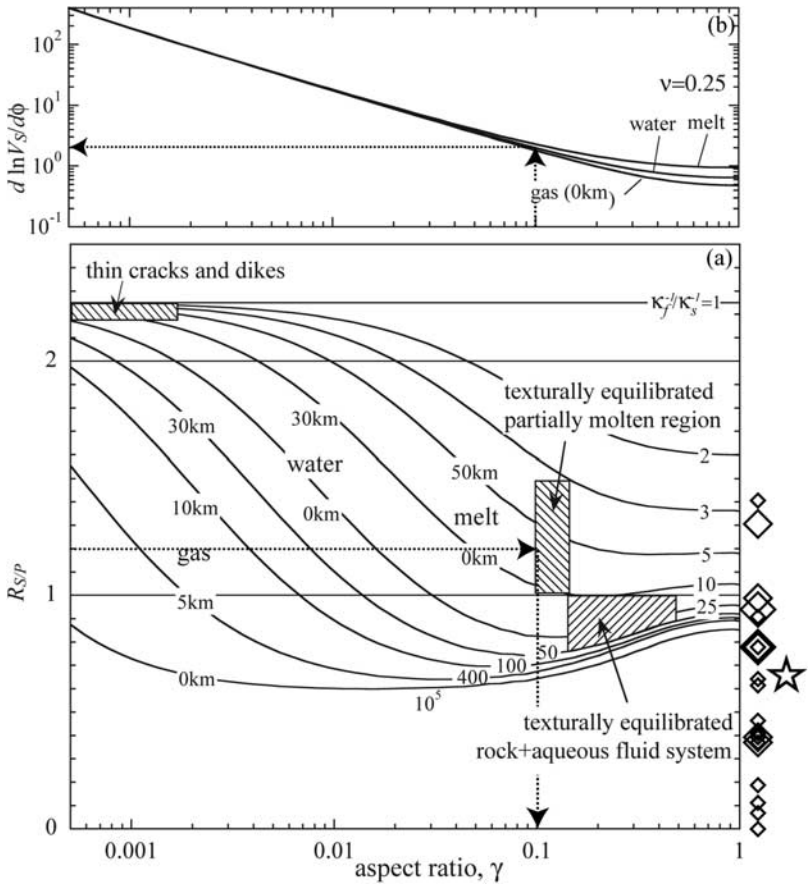

Figure 12. (a) $R_{S/P}$ versus aspect ratio of the pore. The star indicates the value of $R_{S/P}$, as estimated from the slope of the fitting line in Figure 11b. Diamonds indicate values of $R_{S/P}$, as calculated for each data point in Figure 11b. The size of each diamond indicates the absolute value of $d\ln V_S$, with larger symbols representing data that are more reliable. Using a value of $R_{S/P} = 1.2$ and $\kappa_f^{-1}/\kappa_s^{-1} = 7$, the aspect ratio is obtained to be $\gamma = 0.1$. (b) Plot of $d\ln V_S/d\phi$ versus aspect ratio of the pore. For $\gamma = 0.1$, we obtain $d\ln V_S/d\phi = \sim 2$. Further explanation of this diagram is given by *Takei*'s (2002) Figure 5.

1000) and negative traveltime anomalies ($-0.07 < d\ln t_{P,S} < -0.01$). The Pacific mantle data show low- to moderate-attenuation anomalies ($1000 > Q_P > 250$) and negative or absent traveltime anomalies ($-0.05 < d\ln t_{P,S} < 0.00$).

[31] The relations between the observed attenuation and traveltime anomalies of the slab and the Pacific mantle data are consistent with those predicted theoretically on the basis of the thermal effect. In contrast, the mantle wedge data

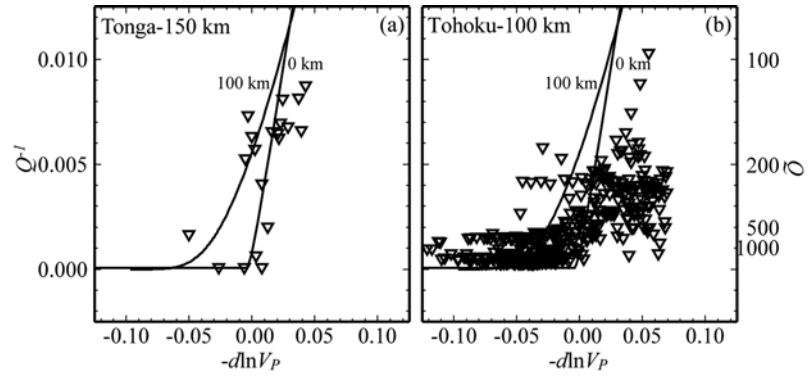

Figure 13. (a) Relation between the attenuation and traveltime anomalies in the Tonga subduction zone. The data are obtained from tomographic models of P wave attenuation [*Roth et al.*, 1999] and P wave velocity [*Zhao et al.*, 1997]. (b) Relation between the attenuation and traveltime anomalies in Tohoku subduction zone. The data are taken from tomographic models of P wave attenuation [*Tsumura et al.*, 2000] and the P wave velocity [*Nakajima et al.*, 2001].

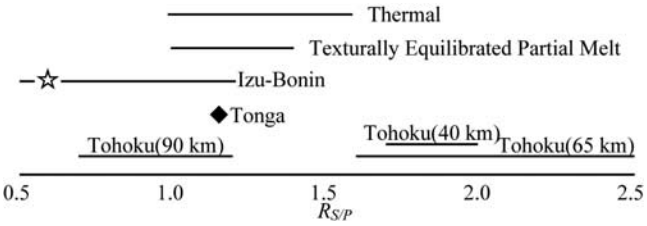

Figure 14. Summary of seismological observations and theoretical and experimental results with respect to $R_{S/P}$.

show pronounced positive traveltime anomalies unaccompanied by comparable high attenuation, inconsistent with an explanation solely in terms of the thermal effect. The temperature anomalies estimated from attenuation data indicate that the temperatures in the mantle wedge exceed the dry solidus of peridotite, suggesting in turn the existence of partial melt in the mantle wedge. The value of $R_{S/P}$ estimated from the slope of the fitting line calculated for 26 traveltime anomaly measurements in the mantle wedge is 0.93 before correction of the thermal effect and 0.64 after correction. The values of $R_{S/P}$ estimated for each pair of P and S ave traveltime anomalies fall in the range 0.5–1.2, much less than the value expected for the thermal effect ($R_{S/P}$ = 1.38). Although values of $R_{S/P}$ between 1.0 and 1.5 are explained by the presence of textually equilibrated partial melt, values less than 1.0 are difficult to be explained in terms of malt. Further studies are required that taking into account the possible effect of anisotropy on seismic wave velocities.

[32] **Acknowledgments.** We thank Douglas Wiens, Junichi Nakajima, and Noriko Tsumura for their constructive comments and providing tomography data. We acknowledge Shun-ichiro Karato, Takashi Yoshino, and Koki Aizawa for their thoughtful comments. We thank Claudia Adam for careful reading of the manuscript and useful comments. We also thank two anonymous reviewers and the associate editor for constructive comments that greatly improved the manuscript. We are grateful to the captains, officers, and crew of R/V *KAIREI* for their assistance during the cruises undertaken to deploy and recover the BBOBSs. The high-quality broadband seismogram records were provided by the F-net seismogram network in Japan, operated by the National Research Institute for Earth Science. The figures were produced using GMT software [*Wessel and Smith*, 1998]. This work was supported in part by a Grant-in-Aid for Scientific Research on Priority Areas (KAKENHI, 16075203, 16075208) awarded by the Japan Society for the Promotion of Science and a grant from the 21st Century COE Program awarded by the Ministry of Education, Culture, Sports, Science, and Technology of Japan.

References

Anglin, D. K., and M. J. Fouch (2005), Seismic anisotropy in the Izu-Bonin subduction system, *Geophys. Res. Lett.*, *32*, L09307, doi:10.1029/2005GL022714.

Duffy, T. S., and D. L. Anderson (1989), Seismic velocities in mantle minerals and the mineralogy of the upper mantle, *J. Geophys. Res.*, *94*(B2), 1895–1912, doi:10.1029/JB094iB02p01895.

Dziewonski, A. M., and D. L. Anderson (1981), Preliminary reference Earth model, *Phys. Earth Planet. Inter.*, *25*(4), 297–356, doi:10.1016/0031-9201(81)90046-7.

Faul, U. H., D. R. Toomey, and H. S. Waff (1994), Intergranular basaltic melt is distributed in thin, elongated inclusions, *Geophys. Res. Lett.*, *21*(1), 29–32, doi:10.1029/93GL03051.

Faul, U. H., J. D. F. Gerald, and I. Jackson (2004), Shear wave attenuation and dispersion in melt-bearing olivine polycrystals: 2. Microstructural interpretation and seismological implications, *J. Geophys. Res.*, *109*, B06202, doi:10.1029/2003JB002407.

Fukao, Y., et al. (2009), Stagnant slab: A review, *Annu. Rev. Earth Planet. Sci.*, in press.

Gorbatov, A., and B. L. N. Kennett (2003), Joint bulk-sound and shear tomography for western Pacific subduction zones, *Earth Planet. Sci. Lett.*, *210*(3–4), 527–543.

Hammond, W. C., and E. D. Humphreys (2000a), Upper mantle seismic wave attenuation: Effects of realistic partial melt distribution, *J. Geophys. Res.*, *105*(B5), 10,987–10,999, doi:10.1029/2000JB900042.

Hammond, W. C., and E. D. Humphreys (2000b), Upper mantle seismic wave velocity: Effects of realistic partial melt geometries, *J. Geophys. Res.*, *105*(B5), 10,975–10,986, doi:10.1029/2000JB900041.

Houston, H., and H. Kanamori (1986), Source spectra of great earthquakes: Teleseismic constraints on rupture process and strong motion, *Bull. Seismol. Soc. Am.*, *76*(1), 19–42.

Ita, J., and L. Stixrude (1992), Petrology, elasticity, and composition of the mantle transition zone, *J. Geophys. Res.*, *97*(B5), 6849–6866, doi:10.1029/92JB00068.

Jackson, I. (2000), Laboratory measurement of seismic wave dispersion and attenuation: Recent progress, in *Earth's Deep Interior: Mineral Physics and Tomography From the Atomic to the Global Scale*, *Geophys. Monogr. Ser.*, vol. 117, edited by S. Karato et al., pp. 265–289, AGU, Washington, D. C.

Jackson, I., U. H. Faul, J. D. F. Gerald, and B. H. Tan (2004), Shear wave attenuation and dispersion in melt-bearing olivine polycrystals: 1. Specimen fabrication and mechanical testing, *J. Geophys. Res.*, *109*, B06201, doi:10.1029/2003JB002406.

Kampfmann, W., and H. Berckhemer (1985), High-temperature experiments on the elastic and anelastic behavior of magmatic rocks, *Phys. Earth Planet. Inter.*, *40*(3), 223–247, doi:10.1016/0031-9201(85)90132-3.

Karato, S. (1993), Importance of anelasticity in the interpretation of seismic tomography, *Geophys. Res. Lett.*, *20*(15), 1623–1626, doi:10.1029/93GL01767.

Karato, S., and B. B. Karki (2001), Origin of lateral variation of seismic wave velocities and density in the deep mantle, *J. Geophys. Res.*, *106*(B10), 21,771–21,783, doi:10.1029/2001JB000214.

Kennett, B. L. N., E. R. Engdahl, and R. Buland (1995), Constraints on seismic velocities in the Earth from traveltimes, *Geophys. J. Int.*, *122*(1), 108–124, doi:10.1111/j.1365-246X.1995.tb03540.x.

Koper, K. D., D. A. Wiens, L. Dorman, J. Hildebrand, and S. Webb (1999), Constraints on the origin of slab and mantle wedge anomalies in Tonga from the ratio of S to P velocities, *J. Geophys. Res.*, *104*(B7), 15,089–15,104, doi:10.1029/1999JB900130.

Kushiro, I. (2007), Origin of magmas in subduction zones: A review of experimental studies, *Proc. Jpn. Acad. Ser. B*, *83*(1), 1–15, doi:10.2183/pjab.83.1.

Litasov, K., and E. Ohtani (2002), Phase relations and melt compositions in CMAS-pyrolite-H_2O system up to 25 GPa, *Phys. Earth Planet. Inter.*, *134*(1–2), 105–127, doi:10.1016/S0031-9201(02)00152-8.

Matsukage, K. N., Y. Nishihara, and S. Karato (2005), Seismological signature of chemical differentiation of Earth's upper mantle, *J. Geophys. Res.*, *110*, B12305, doi:10.1029/2004JB003504.

Nakajima, J., T. Matsuzawa, A. Hasegawa, and D. P. Zhao (2001), Three-dimensional structure of V_p, V_s, and V_p/V_s beneath northeastern Japan: Implications for arc magmatism and fluids, *J. Geophys. Res.*, *106*(B10), 21,843–21,857, doi:10.1029/2000JB000008.

Nakajima, J., Y. Takei, and A. Hasegawa (2005), Quantitative analysis of the inclined low-velocity zone in the mantle wedge of northeastern Japan: A systematic change of melt-filled pore shapes with depth and its implications for melt migration, *Earth Planet. Sci. Lett.*, *234*(1–2), 59–70, doi:10.1016/j.epsl.2005.02.033.

Roth, E. G., D. A. Wiens, L. M. Dorman, J. Hildebrand, and S. C. Webb (1999), Seismic attenuation tomography of the Tonga-Fiji region using phase pair methods, *J. Geophys. Res.*, *104*(B3), 4795–4809, doi:10.1029/1998JB900052.

Roth, E. G., D. A. Wiens, and D. P. Zhao (2000), An empirical relationship between seismic attenuation and velocity anomalies in the upper mantle, *Geophys. Res. Lett.*, *27*(5), 601–604, doi:10.1029/1999GL005418.

Shiobara, H., M. Shinohara, M. Mochizuki, E. Araki, and T. Kanazawa (2000), Broad band seismic observation on the sea floor, paper presented at Japan Earth and Planetary Science Joint Meeting, Seismol. Soc. of Jpn. et al., Tokyo, abstract Sd-P001.

Shito, A., and T. Shibutani (2003), Anelastic structure of the upper mantle beneath the northern Philippine Sea, *Phys. Earth Planet. Inter.*, *140*(4), 319–329, doi:10.1016/j.pepi.2003.09.011.

Shito, A., S. Karato, and J. Park (2004), Frequency dependence of Q in Earth's upper mantle inferred from continuous spectra of body waves, *Geophys. Res. Lett.*, *31*, L12603, doi:10.1029/2004GL019582.

Shito, A., S. Karto, Y. Nishihara, and K. Matsukage (2006), Towards mapping the tree-dimensional distribution of water in the upper mantle from velocity and attenuation tomography, in *Earth's Deep Water Cycle*, *Geo-*

phys. Monogr. Ser., vol. 168, edited by S. D. Jacobsen and S. van der Lee, pp. 225–236, AGU, Washington, D. C.

Stachnik, J. C., G. A. Abers, and D. H. Christensen (2004), Seismic attenuation and mantle wedge temperatures in the Alaska subduction zone, *J. Geophys. Res.*, *109*, B10304, doi:10.1029/2004JB003018.

Takei, Y. (2002), Effect of pore geometry on V_P/V_S: From equilibrium geometry to crack, *J. Geophys. Res.*, *107*(B2), 2043, doi:10.1029/2001JB000522.

Tsumura, N., S. Matsumoto, S. Horiuchi, and A. Hasegawa (2000), Three-dimensional attenuation structure beneath the northeastern Japan arc estimated from spectra of small earthquakes, *Tectonophysics*, *319*(4), 241–260, doi:10.1016/S0040-1951(99)00297-8.

Turcotte, D. L., and G. Schubert (1982), *Geodynamics Applications of Continuum Physics to Geological Problems*, Wiley, New York.

Venkataraman, A., and H. Kanamori (2004), Observational constraints on the fracture energy of subduction zone earthquakes, *J. Geophys. Res.*, *109*, B05302, doi:10.1029/2003JB002549.

Webb, S. C. (1998), Broadband seismology and noise under the ocean, *Rev. Geophys.*, *36*(1), 105–142, doi:10.1029/97RG02287.

Wessel, P., and W. H. Smith (1998), New, improved version of Generic Mapping Tools released,, *Eos Trans. AGU*, *79*(47), 579, doi:10.1029/98EO00426. [version 3.1]

Yoshino, T., Y. Takei, D. A. Wark, and E. B. Watson (2005), Grain boundary wetness of texturally equilibrated rocks, with implications for seismic properties of the upper mantle, *J. Geophys. Res.*, *110*, B08205, doi:10.1029/2004JB003544.

Yoshioka, S., and H. Sanshadokoro (2002), Numerical simulations of deformation and dynamics of horizontally lying slabs, *Geophys. J. Int.*, *151*(1), 69–82, doi:10.1046/j.1365-246X.2002.01735.x.

Zhao, D. P., Y. B. Xu, D. A. Wiens, L. Dorman, J. Hildebrand, and S. Webb (1997), Depth extent of the Lau back-arc spreading center and its relation to subduction processes, *Science*, *278*(5336), 254–257, doi:10.1126/science.278.5336.254.

A. Ito and H. Sugioka, Institute for Research on Earth Evolution, JAMSTEC, 2-15 Natsushima-Cho, Kanagawa 237-0061, Japan.

T. Kanazawa, H. Kawakatsu, H. Shiobara, A. Shito, and Y. Takei, Earthquake Research Institute, University of Tokyo, 1-1-1 Yayoi, Bunkyo-ku, Tokyo 113-0032, Japan. (azusas@jamstec.go.jp)